# Amplification of fluorescence from the 3a $^1P^o$ doubly excited state in helium

Š. Krušič,[1,2] K. Bučar,[1] A. Mihelič,[1] and M. Žitnik[1]

[1]*Jožef Stefan Institute, Jamova cesta 39, SI-1000 Ljubljana, Slovenia*
[2]*Faculty of Mathematics and Physics, University of Ljubljana, Jadranska 19, SI-1000 Ljubljana, Slovenia*

We present a theoretical study of self-amplification of extreme ultraviolet light in a helium gas target. Resonant excitation to the $3a$ $^1P^o$ doubly excited state below the $N = 2$ threshold by 100 fs free-electron laser pulses is followed by fluorescence at 40.7 eV photon energy. The process is modeled by a three-level atomic system coupled to the continuum and described by the Maxwell-Bloch equations. The evolution of state populations and radiation fields is studied over a wide range of pump intensities and target pressures, clearly showing the regions of spontaneous emission, amplification, and saturation of light emitted in the forward direction. The treatment includes both coherent and SASE pump pulses. In both cases the amplified pulses are temporally coherent and exhibit a duration similar to that of the pump pulses.

## I. INTRODUCTION

A natural application of intense extreme ultraviolet (EUV) light pulses produced by free-electron lasers (FELs) is nonlinear spectroscopy, where the interest is to study processes triggered by absorption of two or more photons [1–3]. On the other hand, less intense EUV lasers with ultrashort pulse durations, such as higher-order harmonic generation (HHG) sources, are suitable for linear pump-probe spectroscopy, which is able to capture reaction dynamics down to the attosecond time resolution [4]. However, "linear" single photon absorption of radiation from intense EUV sources enables a deposition of a large amount of energy in a very short time, possibly creating an inverted target population that leads to amplification of fluorescence by stimulated emission. With x-ray FELs such as SACLA [5], LCLS [6], and FERMI [7], experiments were performed in the past to induce stimulated emission in various targets such as Ne gas [8] and several solids [9–11]. A few fs long intense FEL pulses were used to create a dense population of the core-hole ionized atoms and consequently a significant amplification of the K-L emission signal was observed in the direction of the pump pulse propagation.

With the aim to produce short coherent pulses the use of another collective effect has been investigated. At the SPring-8 Compact SASE Source superfluorescence from the long-lived $3$ $^1P$ singly excited helium state was observed [12]. Following pumping in the EUV region, pulses with 501.6 nm wavelength as short as 1 ps were reported. The framework for the description of propagation of intense resonant electromagnetic radiation pulses through the medium together with its conversion to the dominant fluorescence decay modes was previously discussed in many details [13–15]. Recently, several theoretical papers have extended the methodology to deal with collective behavior leading to emission amplification in more complex targets, such as HCl and $N_2$ molecules [16,17].

After having studied the theory of amplification of He $2$ $^1P$-$2$ $^1S$ infrared radiation emitted at 2059 nm upon strong pumping of the singly excited $2$ $^1P$ state [18], we extend our studies to the doubly excited states (DES) of helium. Since the early days of research with the synchrotron light it has been known that DES are strongly correlated and decay by autoionization [19]. In the past two decades we have learned about the existence of a weak radiative decay channel where an EUV photon is emitted in the transition from the doubly to the singly excited state in the He atom [20,21].

In our scheme short FEL pulses are used to pump helium gas into the $3a$ $^1P^o$ state, which is at 63.66 eV excitation energy the third lowest-lying doubly excited state of that symmetry above the first ionization threshold. The selected DES is a prototype of a strongly autoionizing resonance with a lifetime comparable to the typical lengths of FEL pulses in the EUV wavelength region ($\sim$100 fs). To investigate the possibility of amplifying the relatively weak DES radiative decay channel emitting 40.7 eV photons with a 5.6 ns$^{-1}$ fluorescence rate, we consider a three-level $\Lambda$ system coupled to two radiation field modes, the pump and the emission field. In addition, several "leakage" processes due to nonresonant photoionization are taken into account. The problem is treated by solving the Maxwell-Bloch equations in time, considering a single spatial coordinate along the propagation direction of the pump pulse.

There exists a number of theoretical studies for systems consisting of several bound states coupled to one or more electromagnetic field modes [22–24]. The study in Ref. [25] deals with the evolution of a two-level system where the upper state decays by autoionization. The closest to our framework are the treatments of the three-level system with one [26] and two autoionizing states [27], but both of them neglect the absorption of the pump field. To our best knowledge, a complete (1D) spatial and temporal evolution of the three-level system coupled to two field modes, where the upper state is an autoionizing resonance, has not been reported before. Such a situation is generally encountered in atomic systems whenever dealing with double electronic excitation of the valence shell
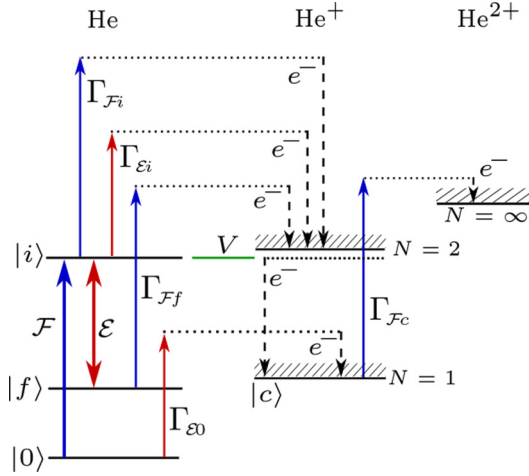
FIG. 1. Schematic representation of the processes after resonant excitation of helium from the ground state $|0\rangle$ to the selected doubly excited state $|i\rangle$. The doubly excited state can decay via autoionization, via fluorescence into the final state $|f\rangle$, or can be photoionized into He$^+$ by the pump or the emitted field. He$^+$ can be further ionized into He$^{2+}$ by the pump field.

or single electronic excitations of the inner-valence shell with tens of eV excitation energy.

## II. SETUP AND FORMULATION

The active medium, i.e., helium gas at a constant pressure, is pumped by FEL pulses with 63.66 eV photon energy resonant with the $1\,^1S^e \rightarrow 3a\,^1P^o$ transition [28]. The excited state with a zero-field lifetime of 80 fs predominantly decays by autoionization. The fluorescence branching ratio is $4.5 \times 10^{-4}$ [29] and the radiative decay occurs with the partial rate $\Gamma_r = 5.6$ ns$^{-1}$. The most probable fluorescence channel populates the singly excited $3\,^1S^e$ state by emission of 40.7 eV photons. As shown in the Appendix, it is the radiative decay channel with the largest branching ratio that gets amplified the most and with the highest probability, making contributions from the competing radiative channels negligible. This is fully

in agreement with the experimental results in the x-ray energy region showing the $K_{\alpha_1}$ amplified emission in Cu to prevail over the $K_{\alpha_2}$ emission [10]. We can thus treat the problem as a three-level system consisting of the ground state of the helium atom (0), the selected doubly excited state ($i$), and the final singly excited state ($f$) (Fig. 1). Operator $V$ describes the coupling between the doubly excited state and the continuum. The states of the three-level system are coupled by two monochromatic and linearly polarized electric fields, pump field $\mathcal{F}$ and emitted field $\mathcal{E}$. In addition to the basic three-level scheme, further nonresonant processes due to the fields are considered: ground-state photoionization by the emitted field is described by rate $\Gamma_{\mathcal{E}0}$, final-state photoionization due to the pump field by $\Gamma_{\mathcal{F}f}$, and excited-state photoionization due to the pump field and the emitted field by $\Gamma_{\mathcal{F}i}$ and $\Gamma_{\mathcal{E}i}$, respectively (Fig. 1). Helium ions can be further ionized into He$^{2+}$ by the pump field, a process described by rate $\Gamma_{\mathcal{F}c}$.

The geometry of the active medium was chosen to be that of a long cylinder with a 5 $\mu$m radius and 1 mm length, which are experimentally achievable parameters and allow for the treatment of the problem in a single spatial dimension [14]. The Fresnel number of the active medium is 4.0 for the FEL light and 2.6 for the emitted light, further justifying the one-dimensional approximation.

The classical electric fields can be written as

$$F(z,t) = \mathcal{F}(z,t)e^{i(k_0 z - \omega_0 t)} + \mathcal{F}^*(z,t)e^{-i(k_0 z - \omega_0 t)}, \quad \text{(1a)}$$

$$E(z,t) = \mathcal{E}(z,t)e^{i(k_f z - \omega_f t)} + \mathcal{E}^*(z,t)e^{-i(k_f z - \omega_f t)}, \quad \text{(1b)}$$

where $\mathcal{F}$ and $\mathcal{E}$ denote their amplitudes, $\omega_0$ and $\omega_f$ their respective frequencies, and $k_0$ and $k_f$ wave numbers in the propagation direction.

We seek the solutions of the time-dependent Schrödinger equation (in atomic units)

$$i\frac{\partial}{\partial t}|\psi(z,t)\rangle = H|\psi(z,t)\rangle. \quad \text{(2)}$$

The effective Hamiltonian operator which describes the atom interacting with the laser field in the rotating wave approximation is written as [30–32]

$$H = \sum_{k=0,i,f}(E_k - i\Gamma_k/2)|k\rangle\langle k| + \int \epsilon_c|c\rangle\langle c|d\epsilon_c + \left(\mathcal{F}(z,t)\mu_{i0}e^{i(k_0 z - \omega_0 t)}|i\rangle\langle 0| + \mathcal{E}(z,t)\mu_{if}e^{i(k_f z - \omega_f t)}|i\rangle\langle f|\right.$$

$$\left. + \int \mathcal{F}(z,t)\mu_{c0}e^{i(k_0 z - \omega_0 t)}|c\rangle\langle 0|d\epsilon_c + \int \mathcal{E}(z,t)\mu_{cf}e^{i(k_f z - \omega_f t)}|c\rangle\langle f|d\epsilon_c + \int V_{ic}|i\rangle\langle c|d\epsilon_c + \text{H.c.}\right), \quad \text{(3)}$$

with $E_k$ being the unperturbed energy of the state $k$, $\epsilon_c$ the energy of the continuum states, $\Gamma_k$ the decay rates of atomic states, $V_{ic} = \langle i|V|c\rangle$, and $\mu_{kj} = \langle k|\mu|j\rangle$, where $\mu$ is the projection of the electric dipole moment onto the field polarization vector.

We write the solutions of Eq. (2) in terms of the slowly varying amplitudes $u_0$, $u_i$, $u_f$, and $u_c$:

$$|\psi(z,t)\rangle = u_0(z,t)e^{-iE_0 t}|0\rangle + u_i(z,t)e^{-iE_0 t + i(k_0 z - \omega_0 t)}|i\rangle + u_f(z,t)e^{-iE_0 t + i(k_0 z - \omega_0 t) - i(k_f z - \omega_f t)}|f\rangle$$

$$+ \int u_c(z,t)e^{-iE_0 t + i(k_0 z - \omega_0 t)}|c\rangle d\epsilon_c. \quad \text{(4)}$$

Following the procedure in Refs. [27,33], we can derive the equations for the spatiotemporal evolution of the density-matrix elements describing the atomic system:

$$\dot{\rho}_{00} = -(\gamma_0 + \Gamma_0)\rho_{00} - 2\,\mathrm{Im}\left[\mathcal{F}\tilde{\mu}_{0i}^*\left(1 + \frac{i}{q_{0i}^*}\right)\rho_{0i}\right], \tag{5a}$$

$$\dot{\rho}_{ii} = -(\Gamma_a + \Gamma_i)\rho_{ii} + 2\,\mathrm{Im}\left[\mathcal{F}\tilde{\mu}_{i0}\left(1 - \frac{i}{q_{i0}}\right)\rho_{0i}\right] + 2\,\mathrm{Im}\left[\mathcal{E}\tilde{\mu}_{if}\left(1 - \frac{i}{q_{if}}\right)\rho_{fi}\right], \tag{5b}$$

$$\dot{\rho}_{ff} = -(\gamma_f + \Gamma_f)\rho_{ff} - 2\,\mathrm{Im}\left[\mathcal{E}\tilde{\mu}_{fi}^*\left(1 + \frac{i}{q_{fi}^*}\right)\rho_{fi}\right], \tag{5c}$$

$$\dot{\rho}_{0i} = -\left(i\Delta_0 + \frac{\Gamma_{0i}}{2} + \Gamma_{0i}^D\right)\rho_{0i} - i\mathcal{F}^*\tilde{\mu}_{0i}\left(1 - \frac{i}{q_{0i}}\right)\rho_{ii} + i\mathcal{F}^*\tilde{\mu}_{i0}^*\left(1 + \frac{i}{q_{i0}^*}\right)\rho_{00} + i\mathcal{E}^*\tilde{\mu}_{if}^*\left(1 + \frac{i}{q_{if}^*}\right)\rho_{0f}, \tag{5d}$$

$$\dot{\rho}_{fi} = -\left(i\Delta + \frac{\Gamma_{fi}}{2} + \Gamma_{fi}^D\right)\rho_{fi} - i\mathcal{E}^*\tilde{\mu}_{fi}\left(1 - \frac{i}{q_{fi}}\right)\rho_{ii} + i\mathcal{E}^*\tilde{\mu}_{if}^*\left(1 + \frac{i}{q_{if}^*}\right)\rho_{ff} + i\mathcal{F}^*\tilde{\mu}_{i0}^*\left(1 + \frac{i}{q_{i0}^*}\right)\rho_{0f}^* + B, \tag{5e}$$

$$\dot{\rho}_{0f} = -\left(i[\Delta_0 - \Delta] + \frac{\Gamma_{0f}}{2}\right)\rho_{0f} - i\mathcal{F}^*\tilde{\mu}_{0i}\left(1 - \frac{i}{q_{0i}}\right)\rho_{fi}^* + i\mathcal{E}\tilde{\mu}_{fi}^*\left(1 + \frac{i}{q_{fi}^*}\right)\rho_{0i}, \tag{5f}$$

where $\Gamma_{0i} = \gamma_0 + \Gamma_0 + \Gamma_a + \Gamma_i$, $\Gamma_{fi} = \Gamma_a + \Gamma_i + \gamma_f + \Gamma_f$, and $\Gamma_{0f} = \gamma_0 + \Gamma_0 + \gamma_f + \Gamma_f$ are the decay widths of the non-diagonal matrix elements, and $\Delta_0 = E_0 + S_0 + \omega_0 - E_i - F_a$ and $\Delta = E_f + S_f + \omega_f - E_i - F_a$ the detunings of the $0 - i$ and $i - f$ transitions, respectively. The widths $\Gamma_0 = \Gamma_{\mathcal{E}0}$, $\Gamma_i = \Gamma_r + \Gamma_{\mathcal{F}i} + \Gamma_{\mathcal{E}i}$, and $\Gamma_f = \Gamma_{\mathcal{F}f}$ describe the spontaneous and photoionization decay rates of the atomic states. For the field-induced ionization shifts and widths of the ground and final state, $S_0$ and $S_f$, and $\gamma_0$ and $\gamma_f$ have been used. The field-induced shifts are of the order of the ponderomotive shifts due to the two fields [26]. For the intensities considered in this work, these are small compared to the spectral width of the pump pulse and the autoionization width of the excited state, and will therefore be neglected in our treatment. Since in our scheme the pump and emitted field are resonant with the $0 - i$ and $i - f$ transitions, respectively, the detunings $\Delta_0$ and $\Delta$ are zero.

The modified dipole matrix elements $\tilde{\mu}_{i0}$, $\tilde{\mu}_{0i}$, $\tilde{\mu}_{if}$, and $\tilde{\mu}_{fi}$ describe the transitions to and from the discrete excited state modified by an admixture of the continuum

$$|\tilde{i}\rangle = |i\rangle + \mathcal{P}\int d\epsilon_c \frac{|c\rangle V_{ci}}{\Delta_\epsilon}, \tag{6}$$

where $\mathcal{P}$ denotes the Cauchy principal value. The real-valued Fano parameters are defined as $q_{i0} = \tilde{\mu}_{i0}/(\pi V_{ic}\mu_{c0})$ and $q_{if} = \tilde{\mu}_{if}/(\pi V_{ic}\mu_{cf})$ [34].

Similar to [18,24], the Doppler line broadening is accounted for in an approximate way by adding an extra decoherence rate $\Gamma_{jk}^D = |E_j - E_k|\sqrt{8\ln 2k_\mathrm{B}T/(Mc^2)}$ to the nondiagonal density matrix elements, with $M$ being the mass of the atoms and $T$ the gas temperature. This is a justified approximation, since the Doppler widths are much smaller than the natural widths of the states and thus the widths of the corresponding Voigt profiles can be approximated by the sum of the two contributions.

The propagation of the pump and the emitted electric field in the target is described by [25]:

$$\left(\frac{\partial}{\partial z} + \alpha\frac{\partial}{\partial t}\right)\mathcal{F}(z,t) = -2\pi i\alpha n\omega_0\tilde{\mu}_{0i}\left(1 - \frac{i}{q_{0i}}\right)\rho_{0i}^*(z,t) - \mathcal{F}(z,t)\left(\frac{n\sigma_{0c}}{2}\rho_{00}(z,t) + \kappa_\mathcal{F}(z,t)\right), \tag{7a}$$

$$\left(\frac{\partial}{\partial z} + \alpha\frac{\partial}{\partial t}\right)\mathcal{E}(z,t) = -2\pi i\alpha n\omega_f\tilde{\mu}_{fi}\left(1 - \frac{i}{q_{fi}}\right)\rho_{fi}^*(z,t) - \mathcal{E}(z,t)\left(\frac{n\sigma_{fc}}{2}\rho_{ff}(z,t) + \kappa_\mathcal{E}(z,t)\right), \tag{7b}$$

where $\sigma_{0c}$ and $\sigma_{fc}$ are the total photoionization cross sections of the ground and final state, respectively. The terms $\kappa_\mathcal{F} = n(\sigma_{\mathcal{F}i}\rho_{ii} + \sigma_{\mathcal{F}f}\rho_{ff} + \sigma_{\mathcal{F}c}\rho_{cc})/2$ and $\kappa_\mathcal{E} = n(\sigma_{\mathcal{E}0}\rho_{00} + \sigma_{\mathcal{E}i}\rho_{ii})/2$ describe field absorption due to the nonresonant photoionization processes. The corresponding photoionization cross sections are defined through $\Gamma_{\xi j}(z,t) = \sigma_{\xi j}|\xi(z,t)|^2/(2\pi\alpha\omega_\xi)$, where $j$ denotes the state being ionized, $\xi = \mathcal{E}, \mathcal{F}$ the electric-field amplitude, and $\omega_\xi$ the corresponding field frequency.

The total population of He$^+$ states, $\rho_+$, can be calculated through its temporal derivative, obtained by summing the partial ionization rates as [27]

$$\dot{\rho}_+ = -\Gamma_{\mathcal{F}c}\rho_+ + \Gamma_a\rho_{ii} + \gamma_0\rho_{00} + \gamma_f\rho_{ff} + \Gamma_{\mathcal{E}0}\rho_{00} + (\Gamma_{\mathcal{F}i} + \Gamma_{\mathcal{E}i})\rho_{ii} + \Gamma_{\mathcal{F}f}\rho_{ff} + 4\,\mathrm{Re}\left(\frac{\mathcal{F}\tilde{\mu}_{i0}}{q_{i0}}\rho_{0i}\right) + 4\,\mathrm{Re}\left(\frac{\mathcal{E}\tilde{\mu}_{if}}{q_{if}}\rho_{fi}\right), \tag{8}$$

and the population of He$^{2+}$ from

$$\dot{\rho}_{2+} = \Gamma_{\mathcal{F}c}\rho_+. \tag{9}$$

Here we have assumed that the cross sections for photoionization of the ground and excited states of the He$^+$ ion are the same. This is a good approximation, since it turns out that the population of the ground state of the He$^+$ ion is much larger than the population of the excited ionic states and so the population of He$^{2+}$ predominantly depends on the photoionization cross section of the ground state of He$^+$.

The set of Eqs. (5) describing the evolution of the density matrix together with the field propagation Eqs. (7) form the so-called Maxwell-Bloch equations. These, together with Eqs. (8) and (9), were rewritten in their finite difference form and numerically propagated on a two-dimensional grid with one spatial dimension [13].

With the phenomenological term $B$ we simulate the effect of fluctuations of the dipole moment which result in the spontaneous radiative decay of the excited state. We define it on a discrete grid of points $(z_m, t_n) = (m\Delta z, n\Delta t)$ as

$$B(z_m, t_n) = A \sum_p e^{i\phi_{mp}} \frac{\delta_{pn}}{\Delta t}, \qquad (10)$$

$$A = \sqrt{\frac{\rho_{ii}\Omega\Gamma_r(\Gamma_a/2 + \Gamma_{if}^D)}{4\pi^2 n\omega_f|\tilde{\mu}_{fi}(1 - i/q_{fi})|^2}}, \qquad (11)$$

with $n$ being the number density of the particles, $\Omega = \pi(r_0/l)^2$ the emission solid angle in the forward direction determined by the dimensions of the medium, and $\delta_{pm}/\Delta t$ the discrete representation of the Dirac delta function $\delta(t_p - t_m)$. The role of the phenomenological term is to impulsively inject a coherence with a phase $\phi_{mn}$, randomly selected from a uniform distribution at each grid point. This term can be written in several different forms [13,15,23]. The one used in our model imposes the relation $\Delta z = c\Delta t$ between the spatial and temporal grid step, which leads to the absence of the grid step size dependence of the normalization factor $A$. The stochastic term defined with Eqs. (10) and (11) has been shown to produce the expected number of emitted photons in the spontaneous emission limit [18]. When it is not convenient to submit the two grid steps to the above mentioned relation, the normalization constant explicitly depends on both of them.

The parameters describing the relevant states and transitions between them are presented in Table I. The energy differences between the states and decay rates are taken from [28,35]. The dipole matrix elements $\tilde{\mu}_{ij}$ and Fano parameters $q_{ij}$, $j = 0, f$, are calculated using the method of exterior

TABLE I. Parameter values (in atomic units) used in the simulations.

| Parameter | Value | Parameter | Value |
|---|---|---|---|
| $\omega_0$ | 2.336 | $\Gamma_{if}^D$ | $9.207 \times 10^{-6}$ |
| $\omega_f$ | 1.497 | $\sigma_{0c}$ | 0.0440 |
| $\tilde{\mu}_{i0}$ | 0.01432 | $\sigma_{fc}$ | $7.43 \times 10^{-4}$ |
| $\tilde{\mu}_{if}$ | 0.2795 | $\sigma_{\mathcal{E}0}$ | 0.1 |
| $q_{i0}$ | $-2.58$ | $\sigma_{\mathcal{E}i}$ | $1.7 \times 10^{-3}$ |
| $q_{if}$ | 309.6 | $\sigma_{\mathcal{F}i}$ | $4.8 \times 10^{-4}$ |
| $\Gamma_a$ | $3.011 \times 10^{-4}$ | $\sigma_{\mathcal{F}f}$ | 0.03 |
| $\Gamma_r$ | $1.358 \times 10^{-7}$ | $\sigma_{\mathcal{F}c}$ | 0.036 |
| $\Gamma_{0i}^D$ | $1.437 \times 10^{-5}$ | | |

complex scaling [27] and the photoionization cross sections $\sigma_{\xi j}$ are estimated using the Atomic Structure Code by Cowan [36]. In the calculations of the photoionization cross sections of the doubly excited state the coupling with the continuum is neglected and the state is treated as bound.

The temporal profile of the incoming FEL pulse is assumed to have a Gaussian intensity profile $I(0, t) = I_0 \exp[-4 \ln 2(t - t_0)^2/\tau_0^2]$ with a full width at half maximum (FWHM) pulse duration $\tau_0 = 100$ fs. The time offset $t_0$, at which the peak intensity $I_0$ of the pump pulse hits the target entrance ($z = 0$), is set to 360 fs. The spatial intensity profile of the pump pulse is assumed to be uniform with a cutoff at $r_0$ (a box-type distribution). Some simulation results are also presented for an axially symmetric Gaussian distribution of pump intensity in the perpendicular plane with the FWHM equal to $2r_0$ and peak intensity $I_0$. The grid step used in the simulations is $\Delta t = \alpha \Delta z = 5$ a.u., which corresponds to 36 nm in space and 0.1 fs in time. The time propagation of the equations was terminated after 9.6 ps, a time which well exceeds the lifetime of the excited state. Because of the random initiation of the emission process, the results of the simulations vary for different sets of phases $\phi_{mn}$ randomly selected for each pulse. In the following, the reported state populations and radiation field profiles are averaged over 20 repeated simulations, unless otherwise stated.

## III. RESULTS AND DISCUSSION

The spectrum of the pump pulse strongly depends on the mode of light production in free-electron lasers, which can be roughly divided into two groups. Seeded FELs, such as FERMI [37], use an external laser source superimposed on the electron beam to induce coherent emission, producing both longitudinally and temporally coherent pulses with a relatively narrow bandwidth. On the other hand, FELs based on self-amplified spontaneous emission (SASE), such as FLASH [38], produce pulses with large shot-to-shot fluctuations of the pulse energy and spectrum and are characterized by low temporal coherence and a relatively large spectral bandwidth [39]. In the following we will investigate the effect of both coherent and partially coherent pumping on the amplification of EUV light in the three-level system.

### A. Coherent pumping

Calculations for the case of coherent pumping were performed over a broad range of target pressures (100–10$^5$ Pa) and pump intensities (10$^{12}$–4×10$^{13}$ W cm$^{-2}$). The number of transmitted FEL and emitted photons in this range is shown in Fig. 2. Several processes are observed: in the limit of low target pressure and pump intensity, the number of emitted photons increases linearly and the emission is spontaneous. Increasing the pump intensity and/or target pressure leads first to the amplification regime with an exponential increase in the number of emitted photons, and finally to the saturation regime, where the dependence of the number of emitted photons on the model parameters $I_0$ and $p$ again becomes linear. At high target pressure the number of both the emitted and transmitted FEL photons decreases, which is a consequence of the absorption of the fields due to the nonresonant photoionization. At the highest investigated pump intensities the
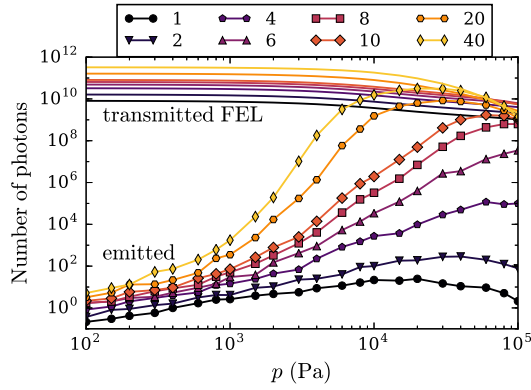
FIG. 2. Number of transmitted FEL and emitted photons as a function of target pressure at different pump intensities after transition through a 1-mm-long He gas target. The pump intensities $I_0$ in the legend are in units of $10^{12}$ W cm$^{-2}$.

number of emitted photons in the saturation regime becomes comparable to the number of transmitted pump photons.

Along with a specific dependence of the number of emitted photons, the temporal and spectral intensity profiles of the corresponding fields also show typical behaviors in the different regimes (Fig. 3). In the spontaneous emission limit, the temporal profile of the emitted pulse exhibits a characteristic exponentially decaying tail and its spectral shape is close to a Lorentzian. The peak of the emitted field intensity is delayed with respect to the pump pulse, because the duration of the latter is comparable to the decay time of the excited state and the transfer of population between the states is mediated by coherences that require a certain time to build up (see the Appendix).

With increasing target pressure or pump intensity, the emitted field becomes strong enough to stimulate the radiative decay of the excited state, leading to an exponential increase in the number of emitted photons in the so-called amplification regime. The delay of the emitted pulse peak increases [18], whereas its duration and spectral shape remain approximately constant. Contrary to the case of spontaneous emission, the profile of the emitted field in the amplification regime is smooth and the random nature of the stochastic term is no longer directly reflected in the intensity profile.

When the population inversion drops to zero, the emitted field saturates and the number of emitted photons again starts
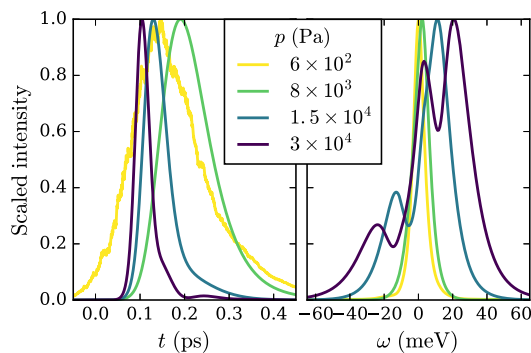


FIG. 3. Temporal and spectral intensity profiles of the emitted field at $I_0 = 2 \times 10^{13}$ W cm$^{-2}$ and different target pressures.

to increase linearly with increasing model parameters. In this regime, the delay of the emitted pulse and its duration decreases with increasing target pressure, which are both characteristic features of superfluorescence [14]. At high target pressures the period of Rabi oscillations on the $i - f$ transition can become shorter than the excited-state lifetime, leading to the appearance of damped oscillations in the temporal profile of the emitted pulse. In its spectral profile a splitting appears, which is due to the dynamic Stark effect [40]. Because the excited state in our scheme is an autoionizing resonance and the pumping is pulsed, the spectrum is complex, exhibiting different numbers of peaks with varying intensity ratios depending on the pump intensity and target pressure [26,41].

Looking at the evolution of the emitted pulse while propagating through the target (Fig. 4), it is clear that the characteristics of the field change similarly with target depth as they do with increasing target pressure or pump intensity. The main parameter determining the evolution of the field is thus the population of the excited state. Since Fig. 4 shows the system evolution for a single pump pulse without averaging, the random nature of spontaneous emission is visible in the initial part of the target, with the temporal [Fig. 4(a)] and spectral intensity profile of the emitted field [Fig. 4(b)] being noisy and the phase of the emitted field [Fig. 4(c)] changing between the grid points, a consequence of the stochastic term (10).

The white dashed line in Fig. 4 corresponds to the saturation condition $\rho_{ii} - \rho_{ff} = 0$. As long as the time at which the system reaches saturation exceeds the time required for the development of the emitted pulse, the number of emitted photons increases exponentially. With increasing target depth the saturation time becomes shorter than the time at which the emitted field intensity reaches its maximum, and the increase in the number of emitted photons becomes linear. With this also the temporal intensity profile of the emitted field changes, exhibiting a shorter delay corresponding to the saturation time.

The presence of Rabi oscillations is also visible in the population inversion map in Fig. 4(d). The position of the maximum of the oscillation in the population inversion, denoted with the dotted line, matches the position of the minimum in the temporal profile of the emitted field. The phase of the emitted field changes by $\pi$ in the course of a Rabi oscillation.

The splitting in the spectral profile of the emitted field [Fig. 4(b)] becomes visible at $z = 0.5$ mm, where the Rabi frequency on the transition between the excited and final state $|\mu_{if}\mathcal{E}(z,t)|$ becomes larger than the decay width of the excited state. This approximately coincides with the transition of the system into the saturation regime. The distance between the peaks in the spectrum increases linearly, corresponding to the linear increase of the Rabi frequency in the saturation regime.

The autocorrelation function of the emitted field

$$g(z, \tau) = \frac{\int_{-\infty}^{\infty} \mathcal{E}(z,t)\mathcal{E}^*(z, t+\tau)dt}{\int_{-\infty}^{\infty} |\mathcal{E}(z,t)|^2 dt} \tag{12}$$

is shown in Fig. 4(e) for the selected example. The coherence time [Fig. 4(f)] is defined as the FWHM of the symmetric correlation function (12). In the initial part of the target, where the emission is spontaneous, the coherence time is
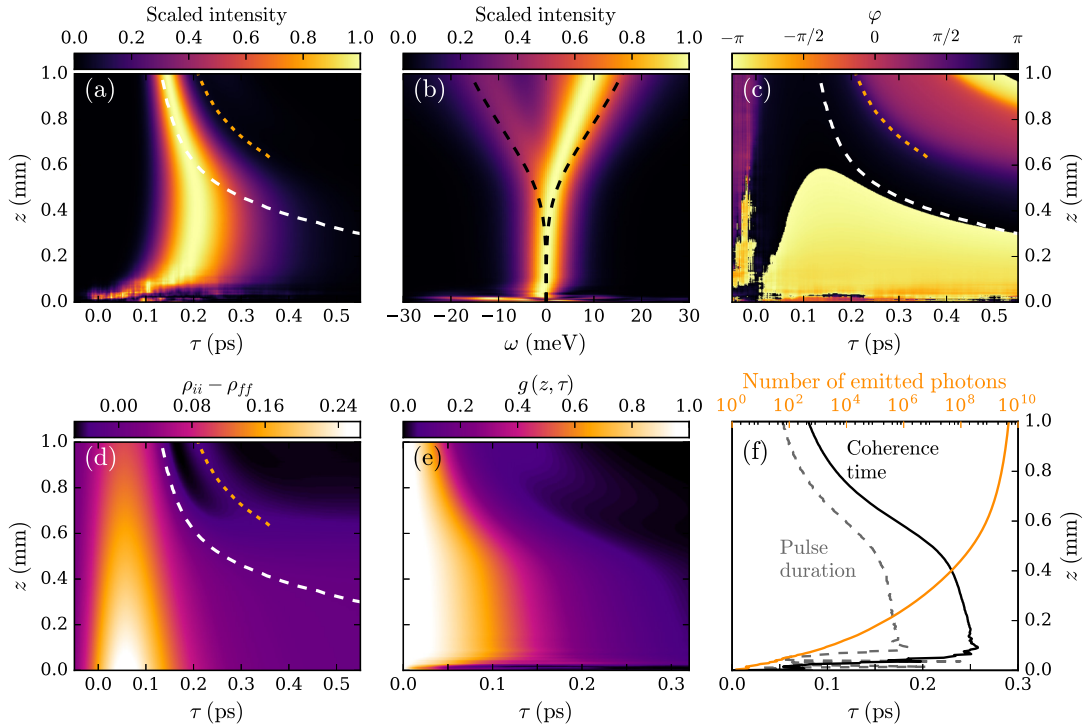
FIG. 4. Evolution of the temporal (a) and spectral intensity profile of the emitted field (b), the temporal profile of the phase of the emitted field (c), population inversion (d), and autocorrelation function of the emitted field (e) in the target at $I_0 = 2 \times 10^{13}$ W cm$^{-2}$ and $p = 1.5 \times 10^4$ Pa for a single pump pulse. The white dashed line denotes $\rho_{ii} - \rho_{ff} = 0$, the dotted line the position of the first oscillation peak in the population inversion, and the black dashed lines the Rabi frequency $\pm |\mu_{if} \mathcal{E}(z,t)|$. The horizontal axis shows the retarded time $\tau = t - z/c$, where $t = 0$ corresponds to the passing of the pump pulse maximum through the target entrance $z = 0$. (f) Number of emitted photons, and duration and coherence time of the emitted pulse as function of the position in the target.

very short due to the random phase of the emitted field. In the amplification regime, the coherence time increases and is larger than the pulse duration, meaning that the emitted pulse is temporally coherent, and the correlation function assumes a Gaussian shape. When the system becomes saturated, the coherence time decreases together with the pulse duration, but the emitted field remains temporally coherent. With the appearance of Rabi oscillations the tails of the correlation function elongate, indicating that the oscillations are indeed phase correlated.

Figure 4(f) shows that at the selected model parameters the number of emitted photons in the amplification regime does not increase entirely exponentially. This is a consequence of strong absorption of the emitted field due to nonresonant photoionization of the ground and doubly excited state at high target pressure.

At low pump intensities, where the transfer of population to the excited state is small, the absorption of the pump pulse follows the Beer-Lamber law [42] with the absorption cross section having the asymmetric Fano shape [34] slightly modified by the presence of Doppler broadening. The Gaussian spectrum of the pump pulse is reshaped into an asymmetric profile exhibiting two peaks [Fig. 5(b)]. At higher pump intensities and target pressures, where the Beer-Lamber law is no longer valid, the spectral intensity of the transmitted pump pulse still decreases systematically with increasing $I_0$ and $p$. The asymmetry of the photoabsorption cross section is also reflected in the temporal profile of the transmitted pump

pulse [Fig. 5(a)], where a secondary peak appears after the main pulse, with its relative intensity increasing with target pressure. At the highest investigated values of $p$, the intensity of the emitted field becomes comparable to the transmitted
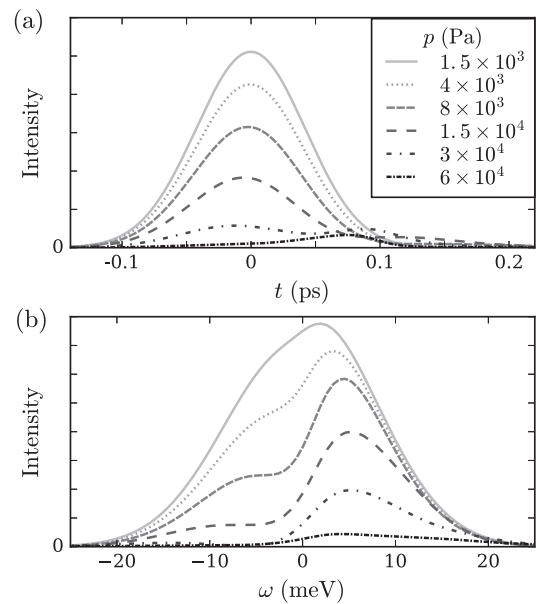


FIG. 5. Temporal (a) and spectral intensity profiles (b) of the transmitted pump pulse at different target pressures and $I_0 = 2 \times 10^{13}$ W cm$^{-2}$.
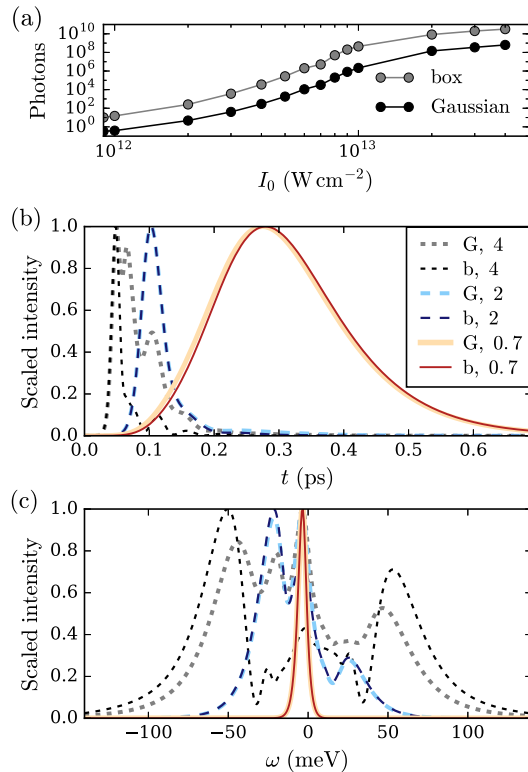
FIG. 6. (a) Number of emitted photons as a function of pump intensity for the box-type and Gaussian spatial intensity distribution at $p = 3 \times 10^4$ Pa. (b) Scaled temporal and (c) spectral intensity profiles of the emitted field at three different pump intensities for the box-type (denoted with b) and Gaussian spatial intensity distribution (denoted with G) at $p = 3 \times 10^4$ Pa. The pump intensities $I_0$ in the legend are in units of $10^{13}$ W cm$^{-2}$.

pump pulse intensity and the two fields are strongly coupled. The coherence time of the transmitted pump pulse is larger than the pulse duration, meaning that the pump pulse remains coherent after passing the target over the whole investigated range of target pressures.

Realistic FEL sources typically produce pulses with a spatial intensity profile that is close to an axially symmetric Gaussian [37]. For an easier comparison of the results obtained for realistic beam profiles we have chosen the Gaussian to have a FWHM equal to $2r_0$ and peak intensity $I_0$. The volume integration was achieved by combining simulation results for the box-type intensity distribution with the same $r_0$. Effectively, a smooth Gaussian profile in the lateral plane was sampled at the selected intensities and the properly weighted box-type results at these intensities were summed up. The results of the spatial averaging are shown in Fig. 6. The number of pump photons is smaller in the case of the Gaussian spatial intensity distribution, and correspondingly so the number of emitted photons. The dependencies of the number of emitted photons on pump intensity for the two distributions are qualitatively the same, with the spontaneous emission, amplification, and saturation regimes visible also with the Gaussian spatial intensity distribution. The temporal and spectral profiles of the emitted field are most affected by the volume integration in the saturation regime. Here the emitted pulse duration is larger, the side peaks in the spectrum
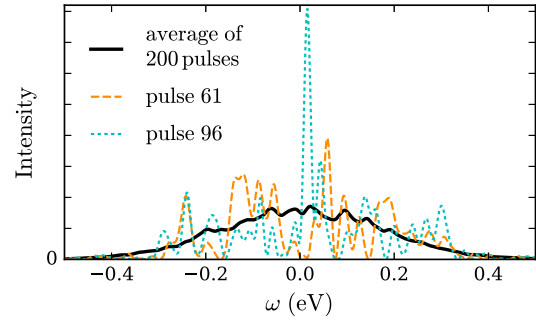


FIG. 7. Spectrum of SASE pump pulses before entering the target for two specific single pulses (pulse number 61 and 96 on Fig. 8) and the average spectrum of 200 pulses.

due to the dynamic Stark effect are less pronounced, and additional structure appears in the area between the peaks, a consequence of the contributions of the box-type simulations at lower pump intensities. In the amplification regime, the temporal and spectral intensity profiles practically coincide with the results for the box-type distribution.

### B. Partially coherent pumping

Pulses produced by SASE FELs can be modeled by a partial-coherence method [43], which uses the information about the average spectral shape and pulse duration to generate sets of light pulses that statistically match the experimentally obtained fields. First, the spectral shape of the pulse is determined, which was chosen to be a Gaussian with a FWHM of 0.4 eV, a spectral resolution achievable with FLASH2 at the selected photon energy [44]. The spectral amplitude of the field is then multiplied by random phases and converted to the time domain by means of the Fourier transform. Finally, the field amplitude in the time domain is multiplied by a Gaussian function with the width corresponding to the duration of the FEL pulse, chosen to be 100 fs, equal to the duration of the coherent pulses from the previous section.

Since the spectral width of the SASE pulses is much larger than that of the coherent pulses, less photons are expected to be absorbed at a given pump intensity, leading to a smaller population inversion which is a key parameter for the development of the emitted pulse. To reach the amplification regime of the emitted field with the partially coherent pumping it is thus necessary to increase the target pressure and pump intensity. Moreover, due to the random generation process of the partially coherent pulses, the shot-to-shot variation is large and the results need to be averaged over a large number of pulses. We will therefore treat the evolution of the system for the case of partially coherent pumping for a single set of model parameters: $I_0 = 4 \times 10^{13}$ W cm$^{-2}$ and $p = 10^5$ Pa.

The random nature of the SASE pump pulses is shown in Fig. 7. The spectral intensity profiles of individual pulses are typically asymmetric and exhibit several peaks with varying heights. As expected, the average spectrum has an approximately Gaussian shape with the width as chosen in the first step of the pulse generation.

Despite each pump pulse having a different spectrum and consequently the number of emitted photons varying strongly between shots, the number of absorbed pump photons is
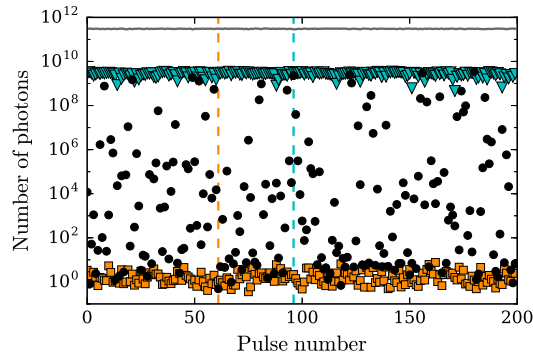
FIG. 8. Number of absorbed pump photons (solid line) and emitted photons (black circles) for different SASE pump pulses. The squares and triangles show the number of emitted photons for different repetitions of the simulation for two specific pump pulses, denoted in the figure with vertical dashed lines and shown in Fig. 7 with the corresponding colors.

approximately constant and much larger than the number of emitted photons (Fig. 8). This indicates that the absorption of the relatively broad pump pulse is mainly due to the nonresonant photoionization. Consequently, the average number of emitted photons per pulse over 200 pump pulses is $1.1 \times 10^8$ and is smaller than the average number of emitted photons in the corresponding case with coherent pumping ($1.4 \times 10^9$) due to the larger spectral width of the SASE pump pulses. The maximal number of emitted photons is $3.5 \times 10^9$, roughly coinciding with the result for coherent pumping. As expected, the case of coherent pumping represents the upper limit for the number of emitted photons. The variation in the number of emitted photons between different shots is around ten orders of magnitude, meaning that in some cases the emission remains spontaneous throughout the whole target, whereas in others the emitted field starts to amplify at different positions or even reaches saturation. The results of different repetitions

of the simulation for the same pump pulse, also shown in Fig. 8, indicate that the number of emitted photons predominantly depends on the spectral shape of the pump pulse and not on the random nature of the spontaneous emission onset.

Figure 9 shows the evolution of the emitted field and population inversion in the target for the two individual pump pulses shown in Fig. 7. The upper row corresponds to the pulse represented in orange, where the emission is spontaneous throughout the target, whereas the lower row shows results for the pump pulse depicted in blue, where the system reaches saturation. There is a strong difference in the temporal dependence of the population inversion. In the first case it consists of several narrow, well separated peaks, whereas in the second case a single wide peak is present, with much smaller population oscillations. Due to the strong absorption of the pump pulse the profile of the population inversion can be strongly modified while traveling through the target. That affects the temporal intensity profile of the emitted pulse, the peak of which moves toward later times together with the position of the maximum of the population inversion. As in the case of coherent pumping, the emitted pulses are coherent in the amplification and saturation regime.

## IV. CONCLUSIONS

We have described the self-amplification of extreme ultraviolet radiation spontaneously emitted after the resonant excitation of helium gas into the selected doubly excited state with short FEL pulses. The three-level scheme is modeled by means of the Maxwell-Bloch equations with an additional stochastic term, which simulates spontaneous emission. The results show that the system transitions from the spontaneous emission limit at low target pressures and pump intensities to the amplification regime, where the number of emitted photons increases exponentially, until it finally reaches saturation. Both in the case of coherent and partially coherent pumping, the pulses emitted along the propagation direction
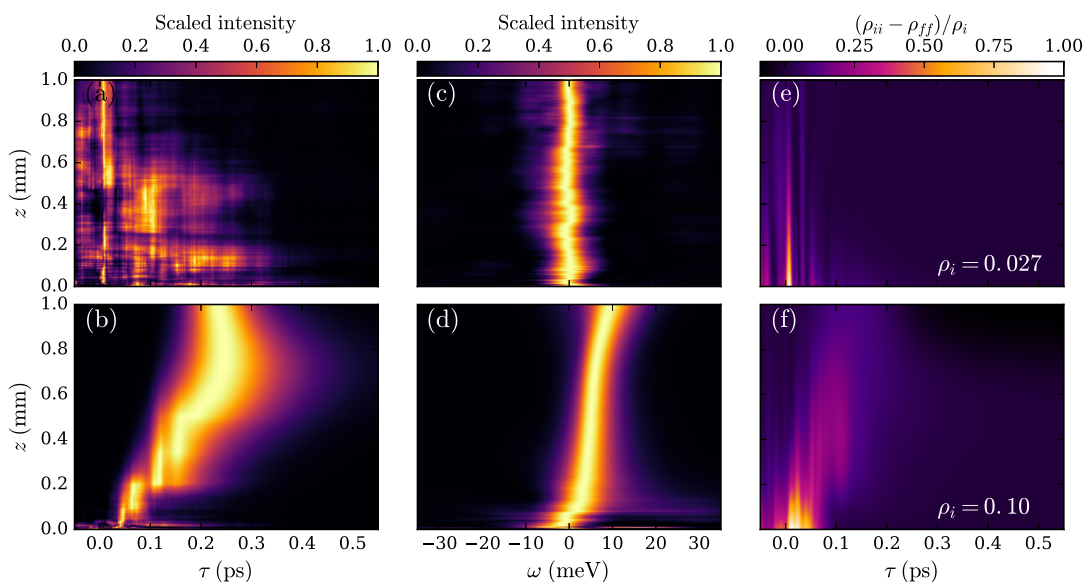


FIG. 9. Evolution of the temporal (a), (b) and spectral intensity profiles of the emitted field (c), (d), and population inversion (e), (f) in the target for two different SASE pump pulses. The upper row shows results for the pump pulse denoted in Fig. 7 with the orange dashed line, and the lower row results for the pulse denoted with the blue dotted line. The scaling factor on figures (e), (f) in defined as $\rho_0 = \max\{\rho_{ii}(0, \tau)\}$.

of the pump pulse are coherent. At high target pressures and pump intensities, the numbers of transmitted FEL and emitted photons are comparable, meaning that the studied system acts as a one-to-two color conversion laser.

Experimentally the amplification of the radiative decay channel could be observed either directly, by recording the spectrum of the emitted radiation in the forward direction, or indirectly, by observing the anomalous increase of the metastable atomic yield produced by the decay of the final singly excited state, by measuring the intensity of the visible light emitted in this decay, or by measuring the decrease of the intensity of the EUV light emitted in the perpendicular direction.

The limitations of the presented theoretical treatment stem mainly from the approximations used in deriving the Maxwell-Bloch equations. The treatment of the problem in a single spatial dimension is valid as long as the saturation length is much larger than the target radius. When these two quantities become comparable, the probability for stimulated emission in the perpendicular direction becomes large and additional spatial dimensions have to be taken into account. At the highest investigated model parameters in this work the saturation length is approximately 60 $\mu$m, still much larger than the target radius.

In this work the numerical results for the 3*a* $^1P^o$ doubly excited state are presented. Other similar resonances in helium differ from this state mainly by the lifetime and branching ratio for the radiative decay. For different selections of the excited state the qualitative characteristics of the emission remain similar; however, the number of emitted photons and the intensity profiles of the emitted field are quantitatively different.

While the treatment includes autoionization of the excited state and nonresonant photoionization of the atomic and ionic states, the emitted field only describes the light emitted by the excited atomic state. The emitted field is nearly resonant with the $1s - 2p$ transition in He$^+$ with transition energy 40.8 eV. At high target pressures, where the population of ionic states in the target is large, the profile of the emitted field could be modified due to the interaction with the ionic states.

The presented scheme offers a possibility of producing monochromatic, short, and coherent light pulses with a well-defined wavelength in the extreme ultraviolet spectral region, corresponding to the dominant radiation decay channel of the upper state prepared by pumping. Running at a high target pressure and pump intensity, such a two-color EUV laser source may be useful because it exhibits a good spatiotemporal overlap of both colors by its nature. In the case of the partially coherent pumping, such as with SASE FELs, the presented scheme offers a complementary approach to the production of coherent pulses.

## APPENDIX

### 1. Two-channel radiative decay of the excited state

The presented amplification scheme assumes the radiative decay of the doubly excited state via a single channel, the one exhibiting the largest partial fluorescence rate. The contributions from other radiative decay channels are neglected and the solution of the problem is sought in the frame of the three-level system. To test the validity of this approximation we have solved an adapted three-level scheme that explicitly accounts for two competing radiative decay paths of the upper state. The two dominant radiative decay channels of the 3*a* $^1P^o$ resonance are populating the singly excited 3 $^1S^e$ and 3 $^1D^e$ states with the respective radiative branching ratios of 76.3% and 20.8% [29]. The branching ratios to other singly excited states are smaller than 1% and these channels are safely neglected. In the simplified problem the target is prepared with all atoms initially in the upper state and nonresonant photoionization is neglected. Thus the upper state is set to decay by three channels: by autoionization and by two radiative decay channels to the 3 $^1S^e$ state (denoted by $f$ as in Sec. II) and the 3 $^1D^e$ state (denoted by $d$). The relevant parameters for the 3*a* $^1P^o \rightarrow$ 3 $^1D^e$ transition are presented in Table II. The three states are treated as pure bound states and autoionization of the upper state is described by a leakage of the excited-state population. The numbers of photons emitted by the 3*a* $^1P^o \rightarrow$ 3 $^1S^e$ and 3*a* $^1P^o \rightarrow$ 3 $^1D^e$ transitions are denoted by $N_1$ and $N_2$, respectively.

The results are compared to the case of a single radiative decay of the excited state, obtained simply by setting the partial decay rate to the 3 $^1D^e$ state to zero. In the latter case the number of photons emitted by the 3*a* $^1P^o \rightarrow$ 3 $^1S^e$ transition is denoted by $N_s$.

The upper graph in Fig. 10 shows that in the amplification and saturation regime the number of photons emitted by the 3*a* $^1P^o \rightarrow$ 3 $^1D^e$ transition is several orders of magnitude smaller than the number of photons emitted by the 3*a* $^1P^o \rightarrow$ 3 $^1S^e$ transition. The ratio $N_1/N_s$ is around 1 over the whole studied target pressure range, with small fluctuations in the low pressure limit due to the random nature of spontaneous emission and averaging over a limited number of pump pulse realizations. This shows that secondary radiative decay channels of the doubly excited state can indeed be neglected in the treatment of the self-amplification scheme.

### 2. Nonprompt excitation

It is interesting to look into the origin of the time delay of model variables when the upper state excitation cannot be

TABLE II. Parameters (in atomic units) relevant for describing the 3*a* $^1P^o \rightarrow$ 3 $^1D^e$ transition.

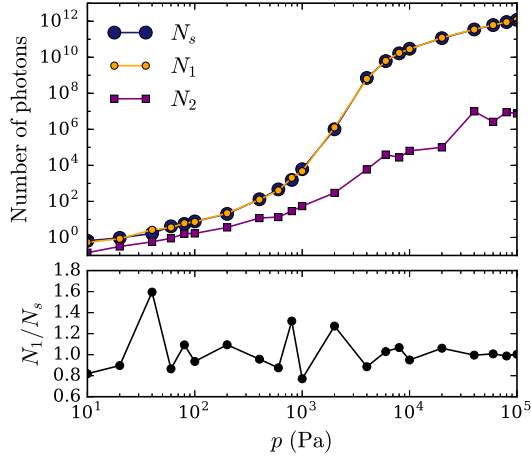| Parameter | Value |
| --- | --- |
| $\omega_d$ | 1.492 |
| $\tilde{\mu}_{id}$ | 0.1469 |
| $q_{id}$ | 738.1 |
| $\Gamma_d$ | $3.710 \times 10^{-8}$ |
| $\Gamma_{id}^D$ | $9.172 \times 10^{-6}$ |
| $\sigma_{dc}$ | $3.60 \times 10^{-5}$ |

FIG. 10. Number of emitted photons on individual transitions as function of target pressure, and the ratio of photons emitted on the $3a\,^1P^o \rightarrow 3\,^1S^e$ transition in the case of the single and double radiative decay of the doubly excited state.

considered prompt, i.e., when the lifetime of the upper state is comparable to the duration of the pump pulse. The situation is most clearly exposed in the weak excitation limit [42]. Assuming $\rho_{00} \approx 1$, $\rho_{ii} \ll 1$ at all times, simple expressions can be obtained for the model time dependence of populations and fields as follows. First, the population of the upper state $\rho_{ii}(t)$ is calculated from the time-dependent pump field $\mathcal{F}$ (assumed to be real). This is done in two steps. Equation (5d) is solved upon neglecting the terms other than the first and the third on the right-hand side. At zero detuning the solution $\rho_{0i}(t)$ of the resulting Langevin equation is proportional to $\mathcal{F} * E[\Gamma_{0i}/2 + \Gamma_{0i}^D]$, the convolution of the pump field with an exponential $E[\Gamma] \equiv e^{-\Gamma t}$. In the next step, Eq. (5b) is solved after neglecting the last term on the right. It is easy to see that $\rho_{ii}(t)$ is proportional to $\{\mathcal{F}(\mathcal{F} * E[\Gamma_{0i}/2 + \Gamma_{0i}^D])\} * E[\Gamma_a + \Gamma_i]$. This differs from $|\mathcal{F}|^2 * E[\Gamma_a + \Gamma_i]$, the rate-equation solution of the same problem, the main difference being that the Maxwell-Bloch solution introduces a time delay in the $\rho_{00} \rightarrow \rho_{ii}$ population transfer because the transition is mediated by the coherence $\rho_{0i}$ that has to build upon the incidence of the pump field. Finally, by inserting the calculated $\rho_{ii}$ time dependence into the (model-dependent) source term (10) and
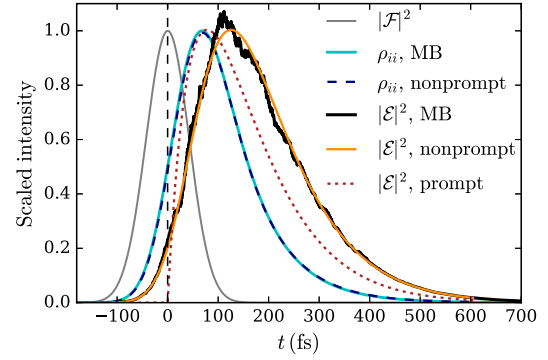


FIG. 11. Development of spontaneously emitted field intensity $|\mathcal{E}|^2$ in time. The upper state is the $3a\,^1P^o$ resonance in He with 80 fs lifetime, excited by the passage of a 100 fs pump pulse $|\mathcal{F}|^2$ through the target. The maximum of the emitted field intensity is delayed for 130 fs with respect to the maximum intensity of the pump pulse. The model result (orange line) is compared to the direct numerical solution of Maxwell-Bloch Eqs. (5) and (7) for the weak excitation case, averaged over 200 pump pulses (black line).

proceeding to calculate the coherence $\rho_{fi}$ along the lines described in Ref. [18], the average emitted field intensity turns out to be proportional to $\rho_{ii} * E[\Gamma_{fi} + 2\Gamma_{fi}^D]$. The time profile of the spontaneous emission intensity in the weak excitation limit therefore converges to

$$\langle|\mathcal{E}|^2\rangle = \left(\{\mathcal{F}(\mathcal{F} * E[\Gamma_{0i}/2 + \Gamma_{0i}^D])\} * E[\Gamma_a + \Gamma_i]\right) * E[\Gamma_{fi} + 2\Gamma_{fi}^D]. \tag{A1}$$

The validity of the above considerations is demonstrated by a good agreement between these convolutions evaluated for the $3a\,^1P^o$ resonance parameters and the direct numerical solution of Maxwell-Bloch Eqs. (5) and (7) for $I = 10^7$ W cm$^{-2}$ and $p = 0.1$ Pa. Figure 11 shows that the population of the upper state and the spontaneously emitted radiation intensity reach their maximum value about 70 fs and 130 fs after the maximum of the pump pulse $|\mathcal{F}|^2$, respectively. When comparing the emitted intensity with the prompt excitation result $E[\Gamma_a + \Gamma_i] * E[\Gamma_{fi} + 2\Gamma_{fi}^D]$ (dotted line in Fig. 11) [18], it is clear that an additional time delay of emission with respect to the pump pulse appears, as noted before [23].

[1] M. Nagasono, E. Suljoti, A. Pietzsch, F. Hennies, M. Wellhöfer, J.-T. Hoeft, M. Martins, W. Wurth, R. Treusch, J. Feldhaus, J. R. Schneider, and A. Föhlisch, Phys. Rev. A **75**, 051406 (2007).

[2] K. L. Ishikawa and K. Ueda, Phys. Rev. Lett. **108**, 033003 (2012).

[3] M. Žitnik, A. Mihelič, K. Bučar, M. Kavčič, J.-E. Rubensson, M. Svanquist, J. Söderström, R. Feifel, C. Såthe, Y. Ovcharenko, V. Lyamayev, T. Mazza, M. Meyer, M. Simon, L. Journel, J. Lüning, O. Plekan, M. Coreno, M. Devetta, M. DiFraia, P. Finetti, R. Richter, C. Grazioli, K. C. Prince, and C. Callegari, Phys. Rev. Lett. **113**, 193201 (2014).

[4] F. Lépine, M. Y. Ivanov, and M. J. J. Vrakking, Nat. Photon. **8**, 195 (2014).

[5] D. Pile, Nat. Photon. **5**, 456 (2011).

[6] P. Emma *et al.*, Nat. Photon. **4**, 641 (2010).

[7] E. Allaria *et al.*, Nat. Photon. **6**, 699 (2012).

[8] N. Rohringer, D. Ryan, R. A. London, M. Purvis, F. Albert, J. Dunn, J. D. Bozek, C. Bostedt, A. Graf, R. Hill, S. P. Hau-Riege, and J. J. Rocca, Nature (London) **481**, 488 (2012).

[9] M. Beye, S. Schreck, F. Sorgenfrei, C. Trabant, N. Pontius, C. Schüßler-Langeheine, W. Wurth, and A. Föhlisch, Nature (London) **501**, 191 (2013).

[10] H. Yoneda, Y. Inubushi, K. Nagamine, Y. Michine, H. Ohashi, H. Yumoto, K. Yamauchi, H. Mimura, H. Kitamura, T. Katayama, T. Ishikawa, and M. Yabashi, Nature (London) **524**, 446 (2015).

[11] P. Jonnard, J.-M. André, K. Le Guen, M. Wu, E. Principi, A. Simoncig, A. Gessini, R. Mincigrucci, C. Masciovecchio, and O. Peyrusse, Struct. Dyn. **4**, 054306 (2017).

[12] M. Nagasono, J. R. Harries, H. Iwayama, T. Togashi, K. Tono, M. Yabashi, Y. Senba, H. Ohashi, T. Ishikawa, and E. Shigemasa, Phys. Rev. Lett. **107**, 193603 (2011).

[13] J. A. Fleck, Jr., Phys. Rev. B **1**, 84 (1970).

[14] M. Gross and S. Haroche, Phys. Rep. **93**, 301 (1982).

[15] O. Larroche, D. Ros, A. Klisnick, A. Sureau, C. Möller, and H. Guennou, Phys. Rev. A **62**, 043815 (2000).

[16] Q. Miao, J.-C. Liu, H. Ågren, J.-E. Rubensson, and F. Gel'mukhanov, Phys. Rev. Lett. **109**, 233905 (2012).

[17] V. Kimberg and N. Rohringer, Phys. Rev. Lett. **110**, 043901 (2013).

[18] Š. Krušič, K. Bučar, A. Mihelič, and M. Žitnik, Phys. Rev. A **98**, 013416 (2018).

[19] R. P. Madden and K. Codling, Phys. Rev. Lett. **10**, 516 (1963).

[20] J.-E. Rubensson, C. Såthe, S. Cramm, B. Kessler, S. Stranges, R. Richter, M. Alagia, and M. Coreno, Phys. Rev. Lett. **83**, 947 (1999).

[21] F. Penent, P. Lablanquie, R. I. Hall, M. Žitnik, K. Bučar, S. Stranges, R. Richter, M. Alagia, P. Hammond, and J. G. Lambourne, Phys. Rev. Lett. **86**, 2758 (2001).

[22] M. G. Raymer, J. Mostowski, and J. L. Carlsten, Phys. Rev. A **19**, 2304 (1979).

[23] C. Weninger and N. Rohringer, Phys. Rev. A **90**, 063828 (2014).

[24] C. Ohae *et al.*, J. Phys. Soc. Jpn. **85**, 034301 (2016).

[25] E. Paspalakis, N. J. Kylstra, and P. L. Knight, Phys. Rev. A **60**, 642 (1999).

[26] S. I. Themelis, P. Lambropoulos, and M. Meyer, J. Phys. B **37**, 4281 (2004).

[27] A. Mihelič, M. Žitnik, and M. Hrast, J. Phys. B **50**, 245602 (2017).

[28] J. M. Rost, K. Schulz, M. Domke, and G. Kaindl, J. Phys. B **30**, 4663 (1997).

[29] J. Söderström, M. Agåker, A. Zimina, R. Feifel, S. Eisebitt, R. Follath, G. Reichardt, O. Schwarzkopf, W. Eberhardt, A. Mihelič, M. Žitnik, and J.-E. Rubensson, Phys. Rev. A **77**, 012513 (2008).

[30] P. Lambropoulos and P. Zoller, Phys. Rev. A **24**, 379 (1981).

[31] G. Alber and P. Zoller, Phys. Rev. A **27**, 1373 (1983).

[32] T. Nakajima and G. Buica, Phys. Rev. A **71**, 013413 (2005).

[33] A. Mihelič and M. Žitnik, Phys. Rev. A **91**, 063409 (2015).

[34] U. Fano, Phys. Rev. **124**, 1866 (1961).

[35] A. Burgers, D. Wintgen, and J. M. Rest, J. Phys. B **28**, 3163 (1995).

[36] R. D. Cowan, *The Theory of Atomic Structure and Spectra* (University of California Press, Berkeley, California, 1981).

[37] E. Allaria *et al.*, J. Synchrotron Radiat. **22**, 485 (2015).

[38] K. Tiedtke *et al.*, New J. Phys. **11**, 023029 (2009).

[39] E. Saldin, E. Schneidmiller, and M. Yurkov, Opt. Commun. **148**, 383 (1998).

[40] S. H. Autler and C. H. Townes, Phys. Rev. **100**, 703 (1955).

[41] M. Lewenstein, J. Zakrzewski, and K. Rzazewski, J. Opt. Soc. Am. B **3**, 22 (1986).

[42] M. Žitnik, Š. Krušič, K. Bučar, and A. Mihelič, Phys. Rev. A **97**, 063424 (2018).

[43] T. Pfeifer, Y. Jiang, S. Düsterer, R. Moshammer, and J. Ullrich, Opt. Lett. **35**, 3441 (2010).

[44] B. Faatz *et al.*, Nucl. Instrum. Methods Phys. Res. A **635**, S2 (2011).